

K2MUSE: A human lower limb multimodal dataset under diverse conditions for facilitating rehabilitation robotics

Journal Title
 XX(X):1–23
 ©The Author(s) 2016
 Reprints and permission:
 sagepub.co.uk/journalsPermissions.nav
 DOI: 10.1177/ToBeAssigned
 www.sagepub.com/



Jiwei Li^{1,2} , Bi Zhang¹ , Xiaowei Tan¹ , Wanxin Chen^{1,2} , Zhaoyuan Liu^{1,2} , Juanjuan Zhang³ , Weiguang Huo³ , Jian Huang⁴ , Lianqing Liu¹ and Xingang Zhao¹

Abstract

The natural interaction and control performance of lower limb rehabilitation robots are closely linked to biomechanical information from various human locomotion activities. Multidimensional human motion data significantly deepen the understanding of the complex mechanisms governing neuromuscular alterations, thereby facilitating the development and application of rehabilitation robots in multifaceted real-world environments. However, currently available lower limb datasets are inadequate for supplying the essential multimodal data and large-scale gait samples necessary for effective data-driven approaches, and they neglect the significant effects of acquisition interference in real applications. To fill this gap, we present the K2MUSE dataset, which includes a comprehensive collection of multimodal data, comprising kinematic, kinetic, amplitude-mode ultrasound (AUS), and surface electromyography (sEMG) measurements. The proposed dataset includes lower limb multimodal data from 30 able-bodied participants walking under different inclines (0° , $\pm 5^\circ$, and $\pm 10^\circ$), various speeds (0.5 m/s, 1.0 m/s, and 1.5 m/s), and different nonideal acquisition conditions (muscle fatigue, electrode shifts, and inter-day differences). The kinematic and ground reaction force data were collected via a Vicon motion capture system and an instrumented treadmill with embedded force plates, whereas the sEMG and AUS data were synchronously recorded for thirteen muscles on the bilateral lower limbs. This dataset offers a new resource for designing control frameworks for rehabilitation robots and conducting biomechanical analyses of lower limb locomotion. The dataset is available at <https://k2muse.github.io/>.

Keywords

Dataset, rehabilitation robot, kinematics, kinetics, lower limb locomotion, multimodal sensing, nonideal condition, A-mode ultrasound, surface electromyography

1 Introduction

Rehabilitation robots, such as autonomous wearable exoskeletons and advanced prostheses, are inherently linked to human locomotion mechanisms [Tan et al. \(2022\)](#); [Chen et al. \(2024a\)](#). The bioinspired system designs and control strategies necessitate that efficient human-robot interaction (HRI) processes rely on abundant biomechanical data derived from motor skills [Elery et al. \(2020\)](#); [Quintero et al. \(2018\)](#); [Kang et al. \(2019\)](#). However, acquiring well-structured human gait data presents significant challenges, as standardized procedures and reliable protocols are needed. Moreover, fully capturing the diverse range of locomotion tasks remains difficult. Existing motion datasets focus primarily on motion analysis and recognition [David et al. \(2023\)](#), revealing a gap between the

available data and their applicability to human-robot coupled systems. To meet the demands of complex human-robot

¹State Key Laboratory of Robotics, Shenyang Institute of Automation, Chinese Academy of Sciences, Shenyang, China

²University of Chinese Academy of Sciences, Beijing, China

³College of Artificial Intelligence, Tianjin Key Laboratory of Intelligent Robotics, Nankai University, Tianjin, China

⁴School of Artificial Intelligence and Automation, Huazhong University of Science and Technology, Wuhan, China

Corresponding author:

Bi Zhang, State Key Laboratory of Robotics, Shenyang Institute of Automation, Chinese Academy of Sciences, No.114 Nanta street, Shenyang, Liaoning 110016, China.
 Email: zhangbi@sia.cn

Xingang Zhao, State Key Laboratory of Robotics, Shenyang Institute of Automation, Chinese Academy of Sciences, No.114 Nanta street, Shenyang, Liaoning 110016, China.

Email: zhaoxingang@sia.cn

coordination scenarios, enhancing the effectiveness and diversity of human motion data is essential.

In the context of robotic system embodiment, exoskeleton controllers should be designed to operate in harmony with the human nervous system to achieve seamless interaction [Wolpert and Kawato \(1998\)](#). To augment motor performance or restore walking ability, human motion data are often used as a reference trajectory for control strategies [Quintero et al. \(2018\)](#); [Kang et al. \(2019\)](#), allowing the control system to manage various rhythmic continuous movements through finite state machines [Young and Ferris \(2016\)](#). However, this control strategy is constrained by predefined assistive modes, making it difficult to generalize this approach to other tasks. Although human-in-the-loop optimization can enhance walking assistive torques and reduce energy costs, it also increases the time burden for participants [Zhang et al. \(2017\)](#); [Ding et al. \(2018\)](#). To overcome these limitations, [Divekar et al. \(2024\)](#) proposed a task-adaptive controller that optimizes performance by dynamically adjusting to specific applications and physiological states. In addition, a different approach to designing control frameworks for multitask and multimodal motion assistance combines the reliability of physical modeling with the adaptability of modern artificial intelligence (AI) [Chen et al. \(2024b\)](#). Further integrating the strengths of multidimensional physiological data and AI would enable exoskeletons to respond more dynamically to various conditions.

Given the unique biomechanics of human movement, data-driven approaches provide alternative solutions to bridge the gap from lab technology to real-world applications, which have demonstrated potential in optimizing the effectiveness of control laws [Slade et al. \(2022\)](#). By utilizing human kinematic trajectory data from [CMU Motion Capture Database \(2024\)](#), optimized exoskeleton controller parameters trained through reinforcement learning algorithms in a simulation environment can facilitate simulation-to-reality (sim2real) motion assistance across multiple scenarios [Luo et al. \(2024\)](#). Data-driven methods can also be employed to establish mapping relationships between wearable sensor data and joint torques [Molinaro et al. \(2024b\)](#). Datasets from various walking tasks have been leveraged to estimate biological joint moments, with the resulting torques serving as control commands for the exoskeleton [Scherpereel et al. \(2023\)](#). By implicitly encoding motion data, the unpredictable nature of human movement can be transformed into an end-to-end model mapping task, realizing the perception and actuation loop [Molinaro et al. \(2024a\)](#). This approach allows the controller to effectively manage interactions between the human, robot,

and environment, thereby enhancing the robustness, scalability, and versatility of the control system. Therefore, datasets with multimodal signals and multiple scenario tasks can support the learning of end-to-end controllers that adapt to biomechanical changes in human motion. This facilitates a symbiotic relationship between humans and robots, endowing the controller with embodied intelligence [Weber and Matsiko \(2023\)](#).

With advancements in medicine, robotics, and AI, research on lower limb locomotion has become progressively more sophisticated. Datasets related to lower limb locomotion have been instrumental in informing this research, as numerous studies have documented the kinematics and kinetics of able-bodied participants engaged in steady-state activities [David et al. \(2023\)](#). These datasets encompass a variety of tasks beyond level-ground walking [Fukuchi et al. \(2018\)](#), including running [Novacheck \(1998\)](#), slope walking [Camargo et al. \(2021\)](#), stair ascent/descent [Riener et al. \(2002\)](#), as well as sitting and standing [Perera et al. \(2024\)](#). In addition, [Reznick et al. \(2021\)](#) and [Scherpereel et al. \(2023\)](#) further expanded the task spectrum by incorporating non-steady conditions and non-cyclic tasks. In tandem with kinematic and kinetic data, signals from other modalities, such as surface electromyography (sEMG), have been explored to measure the activation of specific lower limb muscles [Lencioni et al. \(2019\)](#); [Moreira et al. \(2021\)](#); [Dimitrov et al. \(2023\)](#). These findings provide insights into the physiological changes that occur during movement. These datasets encompass diverse movement patterns across various terrain conditions and walking speeds. Nonetheless, the constraints of the experimental protocols in existing datasets typically limit the availability of multimodal data to a restricted number of strides [Lencioni et al. \(2019\)](#); [Moreira et al. \(2021\)](#); [Dimitrov et al. \(2023\)](#); [Wei et al. \(2023\)](#).

To enhance the diversity and representativeness of datasets, it is crucial to explore a wider range of acquisition paradigms and signal modalities beyond conventional walking tasks. As summarized by [Zhu et al. \(2022\)](#), sEMG, as a characterization of muscle action potentials, is subject to various nonideal conditions arising from different human-robot-environment interactions, such as electrode shifts, muscle fatigue, inter-day differences, and individual variability. These conditions have been less explored in studies of lower limb motion datasets. Investigating these conditions contributes to the laboratory's intention recognition technologies for real-world applications and enhances our understanding of biomechanics. With respect to signal modality, researchers investigating muscle deformation

measurement methods have explored the use of brightness-mode ultrasound to analyze parameters such as the pennation angle and its relationship with joint torque during muscle contraction [Nuckols et al. \(2021\)](#); [Dick et al. \(2017\)](#). Despite advancements in the miniaturization of wearable devices [Wang et al. \(2022\)](#), hardware constraints and computational demands remain significant challenges. Recent advancements in amplitude mode ultrasound (AUS), a lightweight technique for measuring muscle thickness, offer promising solutions for obtaining biomechanical data beyond sEMG and have been widely applied in the recognition of hand and wrist motions [Wei et al. \(2022\)](#); [Yang et al. \(2018, 2022, 2020\)](#). AUS employs one-dimensional scanning to track muscle depth variations, minimizing the dependence on image processing algorithms and complex instrumentation. Therefore, AUS provides a representation of mechanical output by measuring muscle deformation, effectively compensating for the limitations of sEMG, which is susceptible to neurological conditions, thereby improving the insight into muscle physiological mechanisms. However, its application in estimating mechanical loads during continuous lower limb movements remains less explored [Jin et al. \(2024\)](#). In summary, large-scale multimodal datasets that encompass a wide range of complex environments and movement patterns are lacking. This gap limits the availability of comprehensive human motion data and hinders the progression of rehabilitation robotics technology.

In this paper, we introduce an open-source dataset, K2MUSE, which encompasses 20 ambulation conditions and includes comprehensive kinematics, kinetics, amplitude mode ultrasound and surface electromyography data, alongside participants' anthropometric information. The dataset was collected from 30 able-bodied healthy participants. As shown in [Figure 1](#), to connect with daily living settings and encompass a wide range of locomotion modes and conditions, the data collection process involved a variety of locomotion activities, including walking on level ground; ascending walking on 5° and 10° ramps; and descending walking on 5° and 10° ramps. In terms of walking speed, three different speeds were set: 0.5 m/s, 1.0 m/s, and 1.5 m/s. Moreover, the data collection conditions encompassed multiple scenarios, including ideal conditions, muscle fatigue, electrode shifts, and inter-day differences. This dataset is suitable for developing control algorithms for lower limb rehabilitation exoskeletons, active prostheses, and humanoid robots, as well as for intention recognition and biomechanical analysis of lower limb movements. The main contributions of this paper are summarized as follows:

- To our knowledge, this is the first publicly available lower limb motion dataset that simultaneously includes motion capture positions, force plate data, AUS, and sEMG.
- The dataset encompasses up to 20 ambulation conditions, covering a wide range of various inclines and speeds, along with acquisition conditions that account for various nonideal factors.
- A comprehensive reliability assessment and analysis of the dataset were conducted, and its validity was confirmed through comparisons with publicly available datasets and continuous motion estimation experiments.

2 Related work

Human lower limb motion data play a crucial role in the advancement of rehabilitation robots, and various existing datasets have explored a diverse array of walking scenarios and speeds. This section provides a summary of recent lower limb locomotion datasets, as detailed in [Table 1](#).

The variation of the lower limbs in three-dimensional space is a fundamental representation of lower limb ambulation, typically captured via inertial measurement units (IMUs) and camera-based motion capture systems [Luo et al. \(2020\)](#); [Reznick et al. \(2021\)](#). In addition, when combined with kinematic data [Fukuchi et al. \(2018\)](#); [Simonlehner et al. \(2024\)](#), the ground reaction force measured by force plates can be used to derive kinetics. [Luo et al. \(2020\)](#) conducted walking experiments on nine different outdoor surfaces, employing six IMUs to record 3D acceleration and 3D gyroscope data from 30 participants. To obtain kinetic data of the joints, [Fukuchi et al. \(2018\)](#) asked volunteers to walk at self-selected speeds and eight controlled speeds on both overground and treadmill surfaces. However, the data were limited to steady-state tasks. Therefore, [Reznick et al. \(2021\)](#) considered non-steady conditions. Using a motion capture system and force plates, the experimental protocol involved participants walking and running at various speeds and inclines on a treadmill, as well as performing sit-to-stand transitions and stair ascent/descent.

In addition to kinematic and kinetic data, other physiological data have also been included in lower limb datasets, particularly sEMG, which has been widely recorded in numerous datasets [Hu et al. \(2018\)](#); [Schulte et al. \(2023\)](#). The study by [Schwartz et al. \(2008\)](#) addressed the gap in children's data by including multimodal gait data for level ground walking at four different speeds. Similarly, [Moreira et al. \(2021\)](#) reported a dataset from straight walking trials at controlled speeds ranging from 1.0 to 4.0 km/h.

Table 1. Summary of publicly available biomechanics datasets for lower limb locomotion.

Dataset	Acquisition Device	Data Modality	Participant Information			Ambulation Mode	Walking Speed	Ramp Angle
			Total	Male	Female			
Schwartz et al. (2008)	12-camera MCS, force plate, sEMG sensor	kinematics, kinetics, sEMG	83	–	–	LG walking	very slow, slow, self-selected, fast	N/A
Bovi et al. (2011)	9-camera MCS, force plate, sEMG sensor	kinematics, kinetics, sEMG	40	18	22	natural walking, toe-walking, heel-walking, step AS/DS	natural speed, very slow, slow, medium, fast	N/A
He et al. (2018)	ActiCap system (EEG, EOG), goniometers	kinematics, EEG, EOG	8	3	5	threadmill walking	1 mph	N/A
Brantley et al. (2018)	EEG and EMG system, IMU	kinematics, EEG, EMG	10	5	5	LG walking, ramps, stairs.	preferred speed	N/A
Hu et al. (2018)	sEMG system, goniometers, IMU	kinematics, sEMG	10	7	3	sitting, standing, LG walking, ramp AS/DS, stair AS/DS	self-selected speed	10°
Fukuchi et al. (2018)	12-camera MCS, force platform, instrumented treadmill	kinematics, kinetics	42	–	–	LG walking	self-selected speed $\pm 30\%$, 40%–145% of dimensionless speed	N/A
Lencioni et al. (2019)	9-camera MCS, force platform, sEMG recording system	kinematics, kinetics, sEMG	50	25	25	LG walking, toe-walking, heel-walking, step AS/DS	nature speed, increasing/decreasing speed	N/A
Luo et al. (2020)	IMU	kinematics	30	15	15	9 walking surfaces: flat even, up stairs, down stairs, etc	self-selected speed (16.4 \pm 4.2 seconds per trial)	N/A
Reznick et al. (2021)	10-camera MCS, force plates, instrumented treadmill	kinematics, kinetics	10	–	5F	walking, running, ramp AS/DS, sit-to-stand, stair ascent/descent	0.8–2.4 m/s	5°, 10°
Camargo et al. (2021)	Vicon system, goniometers, IMU, force plate, sEMG sensor	kinematics, kinetics, sEMG	22	–	–	LG walking, ramp ascent/descent, stair ascent/descent	slow, normal, fast, 0.5–1.85m/s	5.2° – 18°
Moreira et al. (2021)	12-camera MCS, force platform, sEMG system	kinematics, kinetics, sEMG	16	8	8	LG walking	1.0–4.0 km/h	N/A
Wei et al. (2023)	6-camera MCS, force platforms, sEMG acquisition system	kinematics, kinetics, sEMG	40	30	10	LG walking, walking up/downstairs, etc.	comfortable speed	N/A
Schulte et al. (2023)	IMU, sEMG system	kinematics, sEMG	55	25	30	sitting, standing, walking, stair ascent/descent, ramp ascent/descent, etc.	preferred speed	N/A
Sharma et al. (2023)	IMU, eye tracker	kinematics, vision and gaze data	76	39	37	LG walking, unrestricted walking in public spaces, controlled obstacle course.	self-selected speed	N/A
Ortiz et al. (2023)	EEG, EOG, EMG acquisition system	EEG, EOG, EMG	14	9	5	LG walking, ramp walking	depend on the exoskeleton	N/A
Dimitrov et al. (2023)	10-camera MCS, force platform, IMU, EMG sensor	kinematics, kinetics, HDsEMG	10	5	5	LG walking, ramp walking, stair ascent/descent, sidestepping, etc.	slow, preferred, fast	5°, 15°
Van Crielinge et al. (2023)	8-camera MCS, force plate, sEMG system	kinematics, kinetics, sEMG	188	99	89	LG walking	self-selected speed	N/A
Scherpereel et al. (2023)	33-camera MCS, instrumented treadmill, force plates, EMG sensor	kinematics, kinetics, sEMG	12	7	5	31 tasks include walking running, jumping, sit-to-stand, etc.	0.6 m/s - 2.5m/s	5°, 10°
Perera et al. (2024)	mocap system, force plate, EMG sensor, IMU	kinematics, kinetics, sEMG	65	23	42	Sit-to-walk	N/A	N/A
Simonlehner et al. (2024)	12-camera MCS, force plate	kinematics, kinetics	20	9	11	LG walking	self-selected speed	N/A

Note: MCS – motion capture system; LG – level ground; AS – ascending; DS – descending.



Figure 1. Experiments were conducted in the biomechanics laboratory. (a) The experimental scene shows a participant equipped with all the devices: a motion capture system, a treadmill with embedded force plates, an sEMG system, and an AUS device. (b) Participants performed experiments on a treadmill under diverse conditions, including different ascending and descending ramps and walking speeds. In the fatigue-induced experiment, the participants alternated between squatting and walking continuously.

In addition to walking at different speeds, the dataset proposed by [Bovi et al. \(2011\)](#) and [Lencioni et al. \(2019\)](#) included various other walking modes, such as toe-walking, heel-walking, and step ascending/descending. [Camargo et al. \(2021\)](#) reported kinematic, kinetic, and sEMG data from walking trials at various speeds and slopes and included information from IMUs and goniometers. [Perera et al. \(2024\)](#) focused on sit-to-stand transitions, and recorded kinematics, kinetics, IMU, and sEMG data from multiple joints. [Dimitrov et al. \(2023\)](#) reported kinematic, kinetic, IMU, and high-density sEMG data for various tasks, such as walking at different speeds, ramp ascent/descent, sit-to-stand-to-walk, stair ascent/descent, and side-stepping gaits. To expand the number of walking tasks included in the dataset, [Wei et al. \(2023\)](#) and [Scherpereel et al. \(2023\)](#) designed 16 and 33 different motion tasks, respectively, to capture the diversity of lower limb movements. These datasets include kinematic, kinetic, and sEMG data for both

cyclic and non-cyclic activities. [Van Criekinge et al. \(2023\)](#) made significant contributions in terms of participant scale, reporting self-selected speed walking data from 138 healthy adults and 50 stroke survivors. In addition to sEMG, other biological signals, such as electroencephalography (EEG) [Ortiz et al. \(2023\)](#); [Brantley et al. \(2018\)](#), electrooculogram (EOG) [He et al. \(2018\)](#), and egocentric data [Sharma et al. \(2023\)](#), have also been recorded to capture physiological changes during walking.

To our knowledge, no existing dataset simultaneously includes the following: kinematic and kinetic recordings, multimodal physiological signal measurements, trials under nonideal conditions, and large-scale walking data sufficient for data-driven methods. To address these challenges, we release a novel lower limb motion dataset that includes comprehensive multimodal data across various walking speeds and ramps. This dataset aims to promote

further advancements in rehabilitation robotics and intention recognition.

3 Methods

3.1 Participants

This dataset was acquired from thirty healthy participants: twenty males, ten females, ranging in age from 22–34 years (25.97 ± 2.39), height from 145.2–186.7 cm (172.95 ± 9.42), and weight from 42.65–113 kg (69.65 ± 15.04). The participants were recruited from the Shenyang Institute of Automation, Chinese Academy of Sciences. None of the participants reported any neurological diseases or musculoskeletal dysfunctions that could affect lower extremity motor performance. The experimental protocol was approved by the Ethics Committees of the Shenyang Institute of Automation, Chinese Academy of Sciences, and the People's Hospital of Liaoning Province, China (2023-MSLH-117), and was conducted in accordance with the Declaration of Helsinki. All participants were briefed about the procedures and potential risks and provided written, informed consent before participating in the experiment.

3.2 Instrumentation

Data were collected in the Biomechanics Laboratory at the Shenyang Institute of Automation, Chinese Academy of Sciences. The laboratory is equipped with a motion capture system, an instrumented treadmill, an sEMG acquisition system, and an amplitude mode ultrasound acquisition system to collect kinematic, kinetic, and biological signals from various movements. Data synchronization between different devices was achieved through the square wave voltage signal generated by the Vicon Lock Lab. The placement of retro-reflective markers and sensors was always performed by two experienced assessors. The final placement was determined after a consensus was reached.

3.2.1 Treadmill. All walking trials were conducted on a fully instrumented treadmill (Bertec, Columbus, Ohio). The treadmill features two independently controllable belts, each equipped with a force plate underneath to capture six-component force data at 1000 Hz. The treadmill incline was configured via software, and its start/stop functions, and speed were controlled by custom MATLAB code. The treadmill acceleration was consistently set to 0.25 m/s^2 in all the acquisition experiments.

3.2.2 Motion capture. Three-dimensional kinematic trajectories of retro-reflective markers (14 mm diameter) were recorded at 100 Hz via a motion capture system consisting

of eight Vicon V5 cameras (Vicon, Oxford, UK). Before the formal experiments commenced, motion capture volume calibration of the cameras was conducted via a Vicon Active Wand. The Plug-in Gait Model of Vicon was utilized for kinematic and kinetic modeling. Joint angles were calculated on basis of the positions of the markers. The joint forces, moments, and powers were subsequently derived via the kinetics of the force plates and the marker kinematics via the Plug-in Gait Dynamic operation in the Nexus software. A comprehensive description of the Plug-in Gait model, including the specifications of the kinematic and kinetic calculations, can be found in the Vicon Nexus User Guide (Vicon Motion Systems, Inc. (2024a)) and the Plug-in Gait Reference Guide (Vicon Motion Systems, Inc. (2024b)). The placement of the markers followed the Vicon Plug-in Gait lower body model marker set, with an additional set of markers attached to the subjects to improve the fault tolerance of motion capture. These additional markers were used to fill in the missing data frames in the marker trajectories after the acquisition trials. The names and locations of all the markers are shown in Figure 2, with detailed descriptions of specific marker placements available in the Plug-in Gait Reference Guide.

3.2.3 Electromyography. A wireless EMG sensor system (Ultium EMG, Noraxon, USA) was used to record the muscle activity of the bilateral lower limbs at a sampling rate of 2000 Hz. In the hardware setup of MR software (version 3.16, Noraxon, USA), the high-pass and low-pass filter frequencies were configured to 20 Hz and 500 Hz, respectively. The Ultium EMG system was connected to the Vicon Lock Lab via a synchronization system (MyoSync, Noraxon, USA) to receive the synchronous square wave signal. The surface EMG sensors and Ag/AgCl electrodes were affixed to the skin via double-sided tape. The electrode attachment positions were determined through repeated palpation, following the SENIAM recommendations (Hermens et al. (2000)). As shown in Figure 3, the sEMG signals were recorded bilaterally from different muscles, highlighted in blue font. On the right side, 9 muscles were captured: the tibialis anterior (TA), medial gastrocnemius (MG), lateral gastrocnemius (LG), soleus (SOL), rectus femoris (RF), vastus lateralis (VL), vastus medialis (VM), biceps femoris (BF), and semitendinosus (SEM) muscles. On the left side, 4 muscles—TA, LG, RF, and BF—corresponding to the channels of the amplitude mode ultrasound device were recorded.

3.2.4 Amplitude mode ultrasound. A wireless commercial four-channel amplitude mode ultrasound (AUS) device

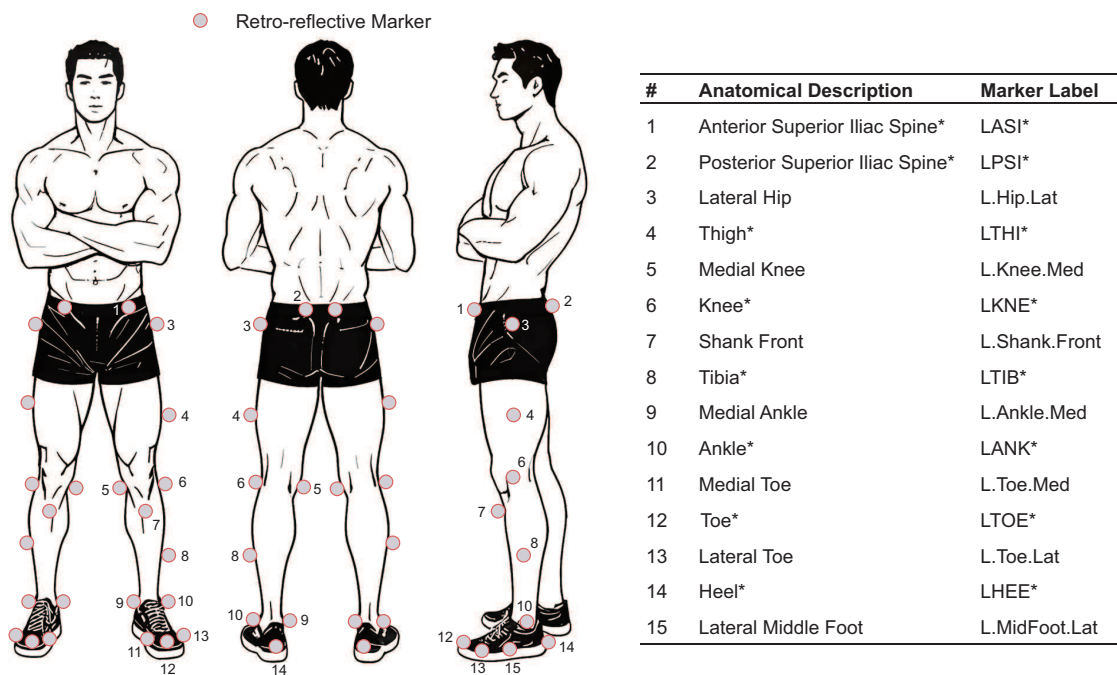


Figure 2. The modified marker set for motion capture. The markers were attached to the lower limbs in a generally symmetrical arrangement, with the markers on the left side shown. Markers marked with “*” were defined according to the Plug-in Gait lower body model, which implements the Conventional Gait Model. Detailed marker placement instructions for the Plug-in Gait lower body model can be found in the Plug-in Gait Reference Guide.

(ELONXI, China) was used to record AUS signals at a sampling frequency of 20 Hz, with each frame containing 1000 samples Wei et al. (2022). The frequency of the transducers was 5 MHz (9 mm diameter, 11 mm height), allowing a detection depth of up to 38.5 mm, which is sufficient for measuring contraction and extension changes within the muscle. To ensure synchronous operation with other devices, the AUS device was connected to the Vicon Lock Lab via a synchronization line to receive the trigger voltage signal. The AUS transducers were coated with an appropriate amount of standard ultrasound coupling agent and then secured to the skin surface of the left leg via PU film medical tape. These transducers corresponded to the TA, LG, RF, and BF muscles, as indicated in yellow in Figure 3.

3.3 Experimental protocol

This study captures kinematic, kinetic, AUS and sEMG data during ambulation at various speeds and inclines under a range of acquisition conditions. All ambulation modes were performed on an instrumented treadmill. A custom MATLAB code was used to control the synchronous start and stop of all device acquisitions. Before each participant arrived, the eight Vicon cameras of the motion capture system were calibrated following the instructions provided in the Vicon Nexus User Guide. The force plates in the Bertec treadmill were hardware reset and zeroed in the Nexus

software. The force plates were recalibrated to zero after the treadmill incline was adjusted.

3.3.1 Participant preparation. After providing informed consent and receiving a brief introduction to all trials, the participants were asked to wear tight-fitting shorts and appropriate athletic shoes to ensure that the transmalleolar axis was exposed. The participant’s top was subsequently secured and tightened with an elastic strap to prevent clothing from obscuring the markers on the pelvis while walking. Before the dynamic capture trials, the following preparations were carried out.

1. The following anthropometric measurements were taken for the Plug-in Gait lower body model: body mass, height, leg length, knee width and ankle width. The measurements were used as inputs for the lower body model, and detailed descriptions are available in the Vicon Nexus User Guide. Comprehensive information about all individuals can be found in the ‘ParticipantInformation.xlsx’ file.
2. Before the placement of the markers and sensors, the hair was removed from the participant’s recording sites, and cotton pads containing 75% alcohol were used to clean the skin surfaces of sweat, keratin, and oil.
3. Sixteen retro-reflective markers were attached to the skin above anatomical landmarks, and additional fourteen

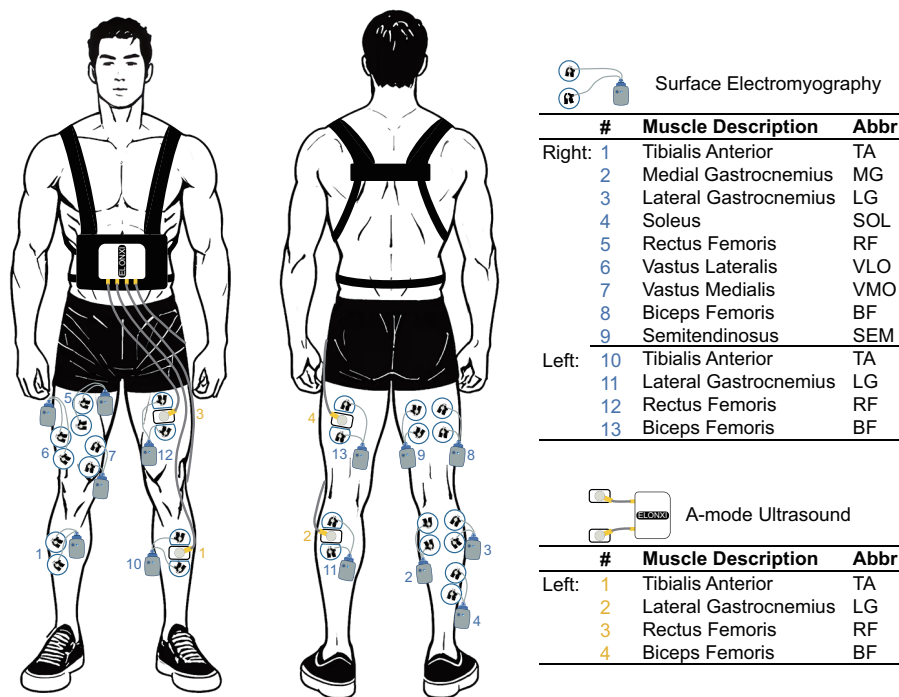


Figure 3. The sEMG sensors and AUS transducers were attached to the participants' skin. The channels of different instrumentation are highlighted in different colors for easy distinction. The symbol '#' corresponds to the channel numbers of different devices.

markers were placed on the lower body through manual palpation. All the markers were securely fixed to the skin using a combination of double-sided tape and PU film medical tape at their base.

4. Thirteen pairs of Ag/AgCl electrodes were attached to muscle locations, and sEMG sensors were placed next to the electrodes using double-sided adhesive tape. The electrodes and sEMG sensors were connected via specially designed electrode wires. PU film medical tape was used to reinforce the electrodes and sensors.
5. Four transducers coated with a coupling agent were placed between paired electrodes, which were trimmed properly to accommodate the transducers. The transducers were connected to the hardware ultrasound system, which was secured to an adjustable vest using elastic bands and hook-and-loop fasteners. The cables were wrapped with non-woven fabric tape to prevent them from being covered by markers during locomotion.

After completing the preparations, a labeling skeleton was created for the participant via the Nexus software, and a static calibration was performed to tailor the skeleton to the participant. The participants were instructed to stand comfortably in the middle of the treadmill with their feet shoulder width apart and positioned on either side of the belt. They maintained an upright posture with their arms crossed in front of their chest to ensure that all the markers were visible. A static trial was then captured, and the calibration

was finalized using a frame where all the markers were fully visible. The collection of dynamic locomotion data for participants was subsequently initiated.

3.3.2 Ideal conditions. All participants in the dataset were involved in the ideal condition experiment. The treadmill inclinations included level ground (LG), descending ramp (DS), and ascending ramp (AS), with angles of 0° , $\pm 5^\circ$, and $\pm 10^\circ$, respectively. The transition between ramps was achieved by altering the participant's orientation on the treadmill, with positive angles for ascending and negative angles for descending. The participants first walked on level ground at speeds of 0.5 m/s, 1.0 m/s, and 1.5 m/s. The treadmill ramp was subsequently adjusted to 5° , and participants walked at -5° and $+5^\circ$ inclines, with speeds of 0.5 m/s and 1.0 m/s for both ramps. Finally, the treadmill incline was adjusted to 10° , and participants walked at -10° and $+10^\circ$ inclines, with speeds the same as those used at 5° . For each ramp, walking tests at each speed were repeated five times, resulting in a total of 55 trials.

3.3.3 Muscle fatigue. After completing all the ideal condition trials, the participants were instructed to rest for 5 minutes before they proceeded with the muscle fatigue experiment. In this section of the experiment, the participants were instructed to walk on level ground at a speed of 1.0 m/s. Between each trial, the participants performed a set of lower limb exercises to induce muscle fatigue, as shown in Figure 4 (a). The participants stood naturally with their feet

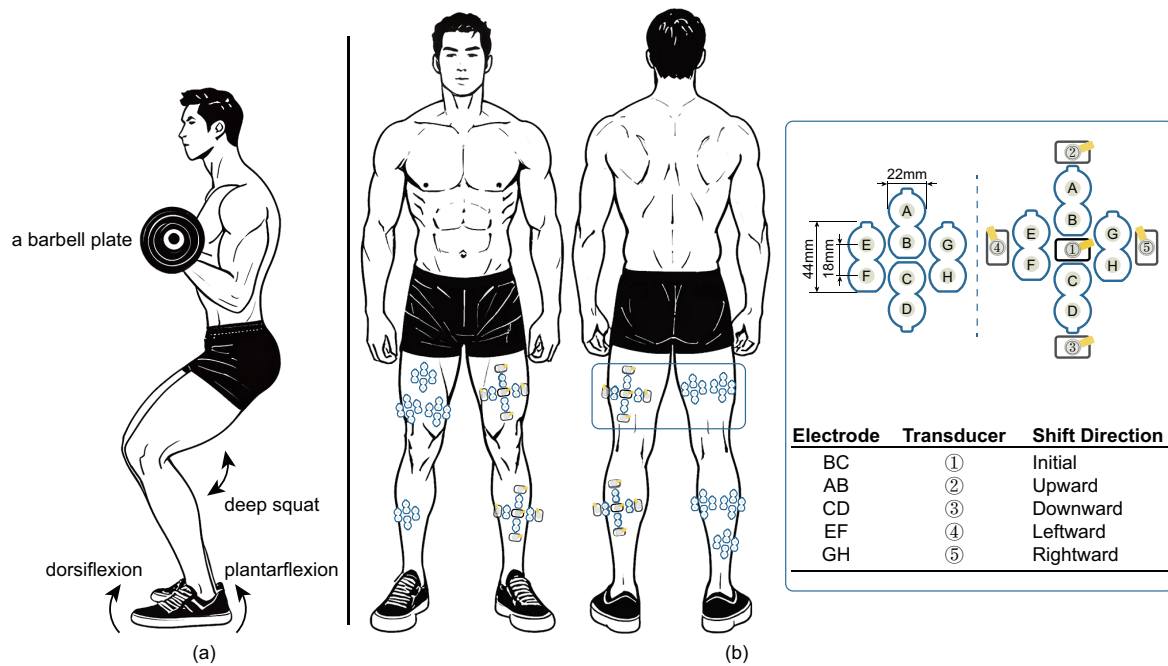


Figure 4. Experimental setups for muscle fatigue and electrode shifts. (a) Fatigue-induced lower limb exercises, including dorsiflexion/plantar flexion and squats, with a barbell held in the hands. (b) Experimental setup simulating electrode shifts, where different electrode pairs and transducers correspond to initial positions and four shift directions.

shoulder-width apart on the ground and held a barbell plate (10 kg for males, 5 kg for females) with both hands. They then performed a complete lower limb exercise, including one repetition of standing plantar flexion and dorsiflexion, followed by one deep squat. After completing 10 full lower limb exercises, the participants immediately returned to the treadmill for the next walking trial without rest. The process was repeated until the participant completed 10 walking trials.

3.3.4 Electrode shift. Eight subjects participated in the electrode shift experiment. This section of the experiment was conducted on a separate day and involved walking on level ground at a speed of 1.0 m/s. As shown in Figure 4 (b), to simulate electrode shifts, an electrode constellation was attached around the muscle bellies. This constellation consisted of four bipolar electrodes arranged symmetrically. The initial electrode position was determined by the difference between B and C, which corresponded to the nominal electrode placement. The shift locations were labeled AB, CD, EF, and GH, corresponding to upward, downward, leftward, and rightward offsets, respectively. The numbers 1 through 5 indicate the positions of the transducers, with their shift directions aligned to match those of the electrodes. The participants first completed the preparation and performed walking trials in the initial position. The assessors then manually adjusted the positions of the differential electrodes and transducers in four directions sequentially and repeated the experimental procedure such

as the initial position. This process continued until five trials were collected for each shift position. A total of 25 trials were recorded for each participant regarding electrode shifts.

3.3.5 Inter-day difference. This section of the experiment also involved eight participants and was conducted on a separate day. It included level-ground walking at speeds of 0.5 m/s, 1.0 m/s, and 1.5 m/s. The placements of the electrodes and transducers, as well as the experimental procedure, were consistent with the ideal experimental conditions, except the effects of manual electrode shifts and muscle fatigue. Each participant completed a total of 15 trials in the inter-day differences experiment. For the eight participants who underwent multiple data collections, the data from the ideal condition of level-ground walking and the initial position data from the electrode shift experiment were also included as part of the inter-day differences data.

3.4 Synchronization procedure

For all conditions, the data collection procedure was the same across all trials. All codes and software were run on the same computer (DELL Precision 7920). Before the start of each trial, the participants were instructed to stand naturally in the middle of the treadmill. The operator modified the values of the variables in the MATLAB code, including the acquisition condition, ambulation mode, treadmill ramp, speed, and trial number (e.g., 'Ideal', 'LG', '0', '1.0', '1'). The MATLAB code sent the start messages to the Nexus software via UDP

communication to trigger data capture, promoting the Nexus software to set the Vicon Lock Lab ports to high voltage (5 V). At this point, the sEMG and AUS devices connected to the Vicon Lock Lab were synchronously triggered to start data acquisition, whereas the MATLAB code established a TCP communication connection with the treadmill. Next, the MATLAB code generated five short beeps, each lasting 1 second, followed by one long beep to signal the participant to get ready. The treadmill was then started according to the speed and ramp parameters. After the participant walked for 40 seconds, the MATLAB code sent stop messages to the Nexus software, causing the Vicon Lock Lab ports to switch to low voltage (0 V). Consequently, all devices stopped collecting data synchronously, and the treadmill ceased operation. Each trial, therefore, included a 45-second data collection period. In addition to the muscle fatigue experiment, the participants were instructed to rest between trials for each condition to avoid fatigue.

3.5 Data Elaboration

3.5.1 Motion capture processing. After data acquisition, motion capture data were processed via Vicon Nexus software (version 2.10, Vicon, Oxford, UK). Retro-reflective markers were labeled and their 3D coordinates were reconstructed. This process allowed the assignment of specified marker names, as illustrated in Figure 2. Trajectory gaps caused by visual occlusion were manually filled using spline fill, pattern fill, rigid body fill, or kinematic fill, depending on the gap length and marker position. The maximum gap length of the spline fill was limited to 20 consecutive frames, and unlabeled marker trajectories were deleted. Further processing was conducted by running the Plug-in Gait Dynamic pipeline in Vicon Nexus. The marker trajectories were filtered via a 4th, zero-lag Butterworth low-pass filter with a cutoff frequency of 6 Hz and a Woltring filter with the MSE mode and a smoothing parameter of 20. The force plate data were filtered via the same Butterworth low-pass filter applied to the marker trajectories. Gait cycle events, including heel strike (HS) and toe-off (TO), were identified for both sides via vertical ground reaction forces (threshold: 20 N) from the force plates and trajectories of the foot markers. The dynamic Plug-in Gait Model subsequently calculated joint kinematics and kinetics by integrating motion capture data with subject-specific anthropometric characteristics. Finally, the processed data were exported as ‘*.c3d’ files, containing joint angles, joint forces, joint moments, joint power, and gait events. Detailed information on motion capture processing is available at the

Vicon Nexus User Guide and the Plug-in Gait Reference Guide.

3.5.2 Data processing. The sEMG data for all participants were stored in the MR software database and exported as ‘*.mat’ files, whereas the AUS data were directly saved as ‘*.txt’ files upon completion of data acquisition. To parse multimodal data into strides and perform time normalization, the participants’ data were compiled into a unified MATLAB structure. Further postprocessing was conducted in MATLAB (version 2022b, MathWorks, Natick, MA, USA). A stride was defined as the motion cycle between two consecutive heel strikes of the same leg. For walking trials, the MATLAB pipeline extracted joint angles, joint forces, joint moments, joint power, and gait events from ‘*.c3d’ files, and parsed the data into strides on the basis of the identified gait events. Each stride was subsequently time normalized by linearly interpolating to 200 data points, ensuring consistent sampling for each gait cycle. To retain steady walking gait cycles for each trial, data collected during treadmill startup were excluded on the basis of the treadmill’s speed, acceleration, and standing time for each trial. Only gait cycles from steady walking were parsed and time-normalized. Then, the ultrasound data from four AUS channels for each trial were extracted and merged from the corresponding ‘*.txt’ files. The ultrasound frames were segmented into cycles based on gait events. Similarly, sEMG data were extracted from individual channels in the ‘*.mat’ files and segmented according to the corresponding gait events on each side of the body. Finally, the processed sEMG and AUS data were merged into the unified MATLAB structure.

4 Dataset Structure

All the data are uploaded to [Kaggle](https://k2muse.github.io/datasets/), and detailed descriptions are available at <https://k2muse.github.io/datasets/>. The K2MUSE dataset comprises kinematic, kinetic, ultrasound, and sEMG data, along with the anthropometric information of participants, as illustrated in Figure 5 (a). The participants’ basic information is stored in a file named ‘ParticipantInformation.xlsx’, which includes details such as ID, gender, birthday, age, height, weight, shoe size, knee width, ankle width, and leg length. The ‘figData.mat’ file contains the average joint angles, joint moments, and joint power values for all participants, which are used to plot the curves in Figure 7.

4.1 Processed data

To facilitate the use of the dataset in this study, all modality data are stored in the ‘*ProcessedData*’ folder. Each participant’s data are organized into a unified MATLAB structure and saved in the format ‘P*.mat’, where ‘*’ corresponds to the participant ID (ranging from 1–30). Each ‘P*.mat’ file follows a standardized field structure, as shown in Figure 5 (b). The ‘P*.mat’ files include kinematic data (3D marker trajectories, 3D joint angles), kinetic data (3D joint forces, 3D joint moments, and 3D joint power), AUS data, sEMG data, and gait events. The ‘OriginalData’ field corresponds to the continuous data for each trial, which were directly extracted from the files exported by different devices without any further processing. The ‘Normalized-Data’ field contains the same data, but they have been normalized by stride and segmented into gait cycles, ensuring consistency and facilitating analysis. The naming convention for the sub-structures of ‘OriginalData’ and ‘NormalizedData’ is organized as follows: (condition).(ambulation mode).(speed).(trial).(datatype). This structure ensures that the data are clearly categorized based on experimental conditions, ambulation modes, walking speed, trial number, and specific datatype. The data structure and descriptions stored in the trial fields of both ‘OriginalData’ and ‘Normalized-Data’ are presented in Table 2 and Table 3, respectively. Further detailed descriptions of the ‘P*.mat’ files in the dataset are available at <https://k2muse.github.io/datasets/>.

4.2 Source data

All raw, unprocessed data are exported and stored in the ‘*SourceData*’ folder. The subfolders within *SourceData*—Vicon, Noraxon, and ELONXI—correspond to data collected by different devices. In the ‘*Vicon*’ subfolder, kinematic and kinetic data are organized in a hierarchical structure of ‘Participant ID/Condition/*.*c3d’. In the ‘*Noraxon*’ subfolder, sEMG data are stored in a hierarchical structure of ‘Participant ID/*.*mat’. In the ‘*ELONXI*’ subfolder, AUS data are organized in a hierarchical structure of ‘Participant ID/Condition/Ambulation Mode/*.txt’. Similarly, more details about the ‘*SourceData*’ folder can be found at: <https://k2muse.github.io/datasets/>.

5 Analysis and Validation

5.1 Reliability of the Plug-in Gait protocol

The Plug-in Gait marker set employed in this study exhibits excellent intra-protocol repeatability and is widely utilized in gait analysis. The primary source of variability arises

from differences in marker placement, which remains the key factor contributing to motion capture discrepancies Gorton III et al. (2009). The marker placement procedure, which is based on anatomical landmarks, was carefully designed to minimize variability. To ensure reliability and consistency, two assessors were responsible for marker placement across the entire dataset. Since two types of tape were used for fixation, marker detachment occurred only in rare cases. If a marker fell off, it was promptly reattached to the exact same position, guided by the imprint left on the skin. The authors utilized the validated Vicon Plug-in Gait model to ensure reliable marker placement Davis III et al. (1991); Grood and Suntay (1983). The standard and widely adopted Plug-in Gait Dynamic pipeline in the Vicon Nexus software was employed for motion data processing, ensuring high reliability Kainz et al. (2017).

5.2 Motion capture and sensor data

Before each experimental session, the motion capture system was calibrated according to the manufacturer’s standard procedure, which involved calibrating the capture volume and setting the volume origin. The system was recalibrated whenever any camera was unintentionally disturbed by external factors. The force plates in the Bertec treadmill were subsequently reset, including leveling the treadmill and setting it to zero level in the Nexus software. The force plates were zeroed in Nexus each time the treadmill incline was changed. The retro-reflective markers, sEMG sensors and AUS transducers were positioned through palpation of bony landmarks and muscle tissue, referring to the guidelines of Hermens et al. (2000) and Rabuffetti et al. (2019). The sEMG and AUS signals were inspected at the beginning of each trial and monitored throughout, ensuring consistent quality.

5.3 Synchronization

Figure 6 presents data collected from different devices during steady-state walking at 1.0 m/s on level ground by a participant, including AUS and sEMG data of the left leg’s rectus femoris (RF), as well as the left hip joint angle. The AUS data utilize a brightness-based method to track variations in muscle thickness Jin et al. (2024). Following the heel strike of the left foot, the hip joint angle decreases from its peak value. During this phase, the left leg supports the body, leading to RF contraction, an increase in muscle thickness, and an increase in the sEMG signal amplitude. As the left hip joint angle reaches its minimum value, the center of gravity shifts toward the right leg. At this point,

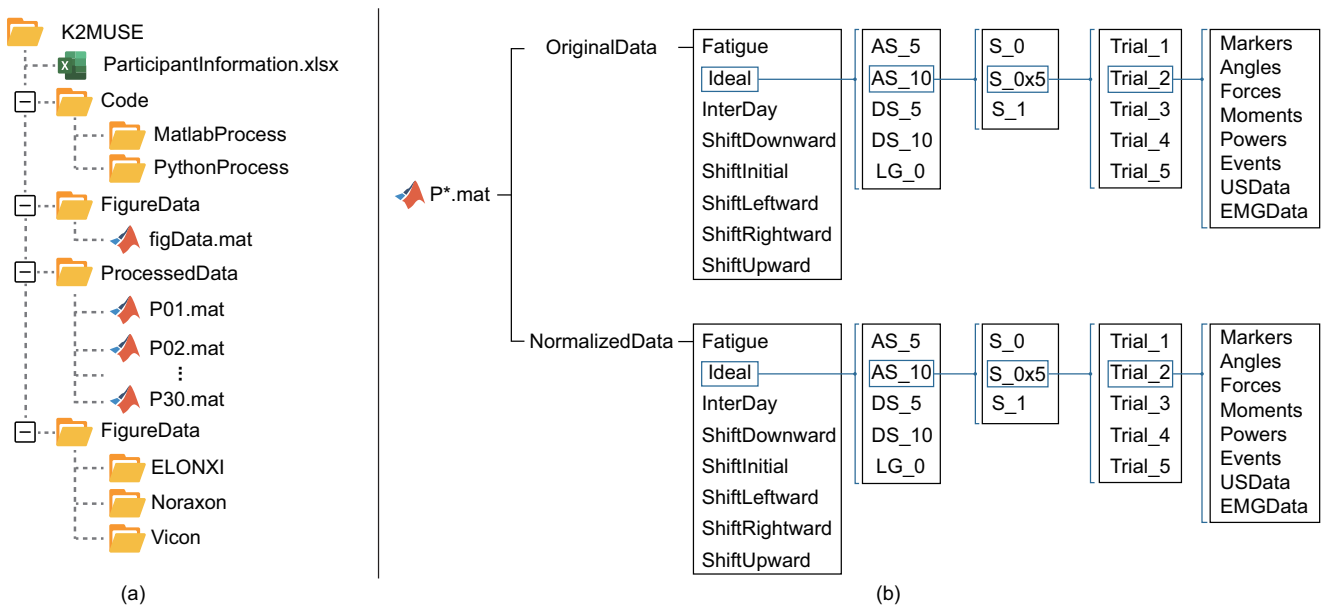


Figure 5. Data organization outlines (a) the folder structure of the dataset and (b) the structured 'P*.mat' file for the participant.

Table 2. Datatype in the 'OriginalData' structure – unprocessed data without parsing or normalizing.

Field within structure	Units	Sampling rate	Contents
Markers	(m)	100 Hz	Positions of the markers defined in Figure 2 in the global coordinate system. Array Format: (total frames \times 3) First Dimension: Frames in trial Second Dimension: x/y/z location in the global space
Angles	(deg)	100 Hz	Pelvic tilt, hip, knee, ankle and foot angles as defined by the Plug-in Gait Model. Array Format: (total frames \times 3) First Dimension: Frames in trial Second Dimension: x/y/z rotation in local space
Forces	(N/kg)	100 Hz	Forces acting on hip, knee, ankle joints, expressed in the local coordinate frame of distal segment. Array Format: (total frames \times 3) First Dimension: Frames in trial Second Dimension: x/y/z joint forces
Moments	(N.m/kg)	100 Hz	Hip, knee, and ankle moments normalized by the participant's mass as defined by the Plug-in Gait model Array Format: (total frames \times 3) First Dimension: Frames in trial Second Dimension: x/y/z joint moments
Powers	(W/kg)	100 Hz	Powers at each joint normalized by the participant's mass, calculated as the multiplication of joint moment and joint velocity. Array Format: (total frames \times 3) First Dimension: Frames in trial Second Dimension: x/y/z joint powers
Events	(s), (Frame)	N/A	Gait events (heel strike and toe-off) detected by force plates in each trial, presented in both time and frame number formats. Array Format: (1 \times HS/TO number) Second Dimension: numbers of gait events.
USData	mm	20 Hz	The extracted and merged AUS data, with frames shaped as (4, 1000), where rows 1 to 4 correspond to transducer channels 1 to 4. Array Format: (total frames \times 1) First Dimension: Frames in trial
EMGData	μ V	2000 Hz	The extracted and merged sEMG data, where columns 1 to 13 correspond to sensor channels 1 to 13. Array Format: (total samples \times 13) First Dimension: Samples in trial Second Dimension: sEMG sensor channels

Table 3. Datatype in the ‘NormalizedData’ structure – data parsed and time-normalized by strides.

Field within structure	Sampling rate	Contents
Markers	(m)	Array Format: $(200 \times 3 \times \text{stride})$
		First Dimension: normalized gait cycle across the stride (200 points)
		Second Dimension: x/y/z location in the global space
		Third Dimension: stride number
Angles	(deg)	Array Format: $(200 \times 3 \times \text{stride})$
		First Dimension: normalized gait cycle across the stride (200 points)
		Second Dimension: x/y/z rotation in local space
		Third Dimension: stride number
Forces	(N/kg)	Array Format: $(200 \times 3 \times \text{stride})$
		First Dimension: normalized gait cycle across the stride (200 points)
		Second Dimension: x/y/z joint forces
		Third Dimension: stride number
Moments	(N.m/kg)	Array Format: $(200 \times 3 \times \text{stride})$
		First Dimension: normalized gait cycle across the stride (200 points)
		Second Dimension: x/y/z joint moments
		Third Dimension: stride number
Powers	(W/kg)	Array Format: $(200 \times 3 \times \text{stride})$
		First Dimension: normalized gait cycle across the stride (200 points)
		Second Dimension: x/y/z joint powers
		Third Dimension: stride number
Events	(Frame)	Array Format: $(1 \times \text{HS number})$
		Second Dimension: stride number
USData	mm	Array Format: $(\text{stride} \times 1)$ First Dimension: stride number
EMGData	μV	Array Format: $(\text{stride} \times 1)$ First Dimension: stride number

the muscle thickness of the left RF reaches its maximum, and the sEMG signal amplitude begins to decrease. Between the current toe-off and the next heel strike of the left foot, the hip joint angle increases because of body inertia. During this period, the muscle does not exert significant force, resulting in a reduction in both muscle thickness and sEMG signal amplitude until the next heel strike occurs. Therefore, according to the above analysis, the simultaneous changes in the joint angle, muscle thickness, and sEMG signal intensity demonstrate synchronization between multiple devices.

5.4 Kinematic and kinetic data

Given that all participants in this dataset are able-bodied and based on the assumption of symmetric kinematics, the presented joint kinematic and kinetic data are derived from the right legs. The joint angles and moments in the sagittal plane under ideal conditions are depicted in Figure 7. Positive joint angle values represent ankle dorsiflexion, knee flexion, and hip flexion, whereas positive joint moment values denote ankle plantar flexion, knee extension, and hip extension. The repeatability of data reflects the consistency in participants’ movements, which directly impacts the

performance of intention recognition and the reliable operation of robotic systems [Wei et al. \(2023\)](#). To ensure this repeatability, the joint angles across participants were validated through the following procedure. First, the mean joint angles were calculated for all gait cycles of each ambulation mode for each participant. Next, the average coefficient of determination (R^2) was computed between the joint angles of each gait cycle and their corresponding mean values. Finally, the R^2 scores for each participant under each ambulation mode were weighted on the basis of the range of motion of the hip, knee, and ankle joints to derive the final $\overline{R^2}$. Figure 8 presents the distribution of $\overline{R^2}$ values for the angles across the five walking modes, with most values exceeding 0.8, demonstrating good repeatability.

5.5 Nonideal condition analysis

According to the description in Section 3.3, the K2MUSE dataset encompasses common nonideal conditions, including muscle fatigue, electrode shifts, and inter-day differences. In this section, we analyze the impact of nonideal conditions on signal acquisition, using sEMG variations as a representative example.

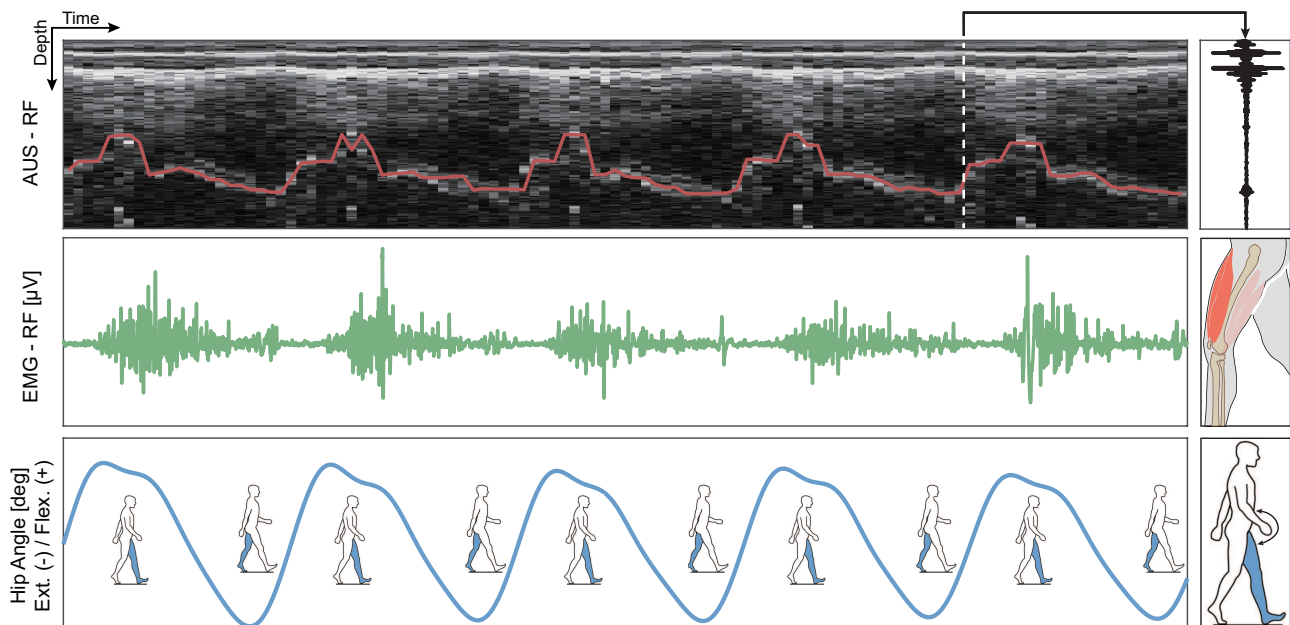


Figure 6. During level-ground walking at 1.0 m/s, the representative AUS and sEMG data of the left rectus femoris (RF), along with the left hip joint angle data, were recorded. The insets on the right side of the AUS data present representative raw AUS data captured at specific time frames.

5.5.1 Muscle fatigue. Muscle fatigue can lead to feature drift in human-machine interfaces, as sEMG-based features are sensitive to fatigue states [Wu et al. \(2016\)](#). The median frequency (MDF) and mean frequency (MF) of sEMG signals are widely recognized as reliable indicators for assessing muscle fatigue, as both have been shown to decrease with increasing levels of fatigue [Chandra et al. \(2018\)](#). Figure 9 depicts the distribution of two frequency features of the left leg RF for a participant throughout each walking trial as the fatigue-enhanced exercise progresses. Starting from the first trial, the distributions of MDF and MF gradually decrease. Although slight increase is observed in the 8th trial, the feature distributions continue to decline in the subsequent two trials. This trend aligns with the findings of [Chandra et al. \(2018\)](#).

5.5.2 Electrode Shifts. To simulate electrode shifts, four offset positions were established in different directions around the initial position. The MAV was selected as the metric for measuring the sEMG amplitudes of the four muscles in the left leg [Zhu et al. \(2022\)](#). As shown in Figure 10 (a), for all five repeated trials of a participant at different shift positions, the maximum muscle action potentials were determined by averaging the maximum MAV values across all gait cycles. For the four muscles, the maximum sEMG amplitudes were recorded at the initial position. The amplitudes for the shank muscles (TA and LG) were smallest at the upward and rightward shift positions, whereas the amplitudes for the thigh muscles (RF and BF) were smallest at the leftward and downward offset positions.

Additionally, Figure 10 (b) illustrates the amplitude variation of LG throughout gait cycles, with the curve for the initial position consistently above those for the other shift positions.

5.5.3 Inter-day difference. The data collection for inter-day differences was conducted on a separate day from the ideal condition. Consequently, a comparative analysis of sEMG under these two conditions was performed. We examined the MAV values of sEMG signals across all gait cycles from five walking trials of a participant at walking speeds of 0.5 m/s, 1.0 m/s, and 1.5 m/s. As shown in Figure 11 (a), for the three walking speeds, the MAV variations throughout the gait cycle exhibit similar trends under both conditions. However, significant amplitude differences are observed, indicating that while the participant's walking pattern remains consistent, the characteristics of the sEMG signal have changed. Specifically, the Euclidean distance shown in Figure 11 (b) provides a quantitative assessment. The intra-condition distances for both the ideal condition and inter-day differences remain relatively small, indicating consistency in the sEMG data characteristics across the five trials within each condition. However, the significantly greater Euclidean distance between the ideal condition and inter-day difference suggests that variations in the participant's physiological state on different days result in notable changes in the sEMG signal characteristics.

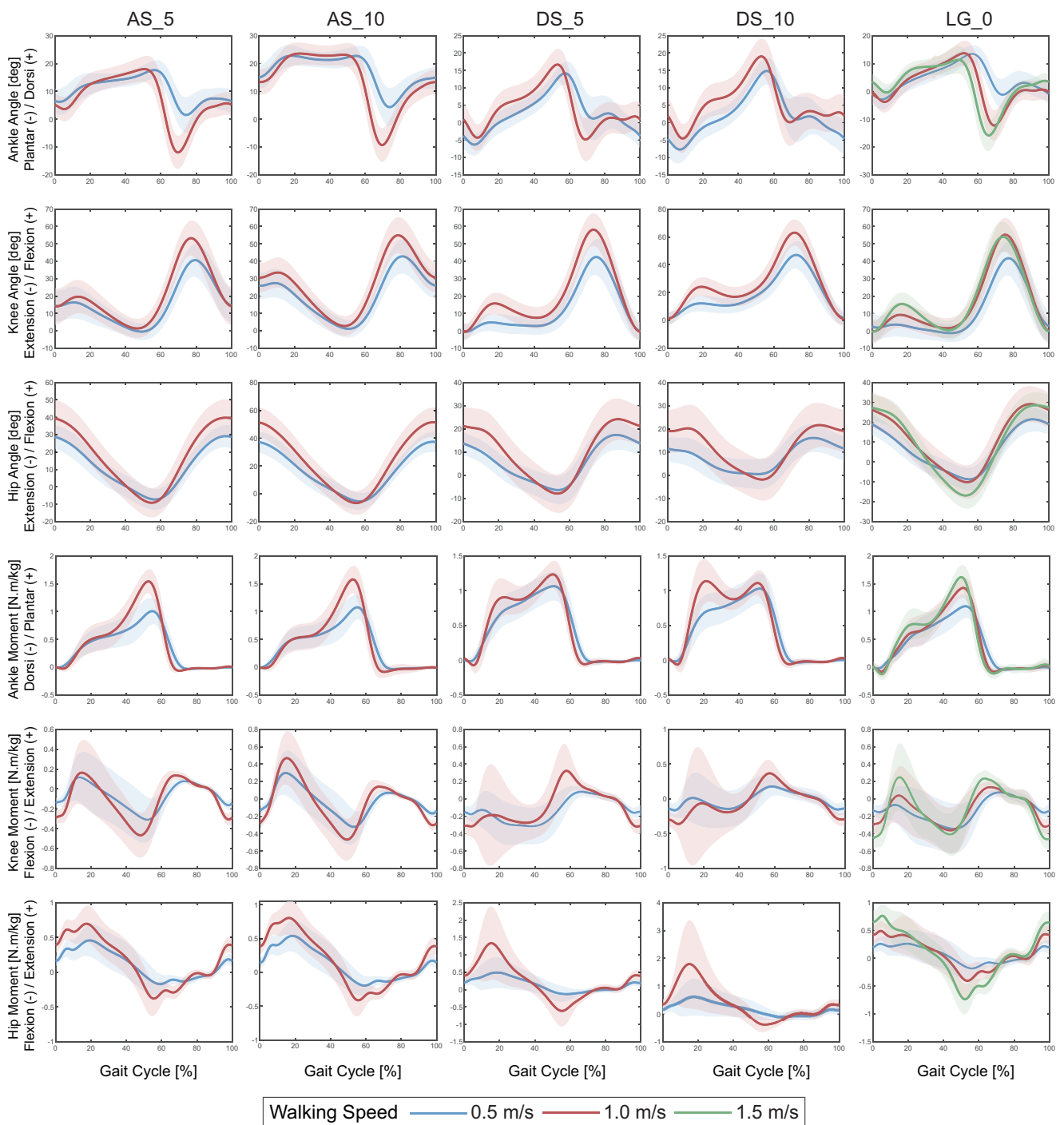


Figure 7. Joint angles and moments during ideal condition experiments. Two consecutive heel strikes correspond to 0% and 100% of the gait cycle. The ambulation mode is annotated at the top. The solid lines indicate the average trajectory across all participants. The shaded regions correspond to the standard deviation.

5.6 Joint angle prediction

To assess the performance of decoding lower limb movements using sEMG and AUS signals, we utilized a support vector regression (SVR) model, a Gaussian process regression (GPR) model, and a multilayer perceptron (MLP) to predict the joint angles of the left leg during level-ground walking at a speed of 1.0 m/s. Given that the focus was not on algorithmic novelty, all the models were implemented via [scikit-learn library](#). For the sEMG data, a

fourth-order Butterworth bandpass filter (20–500 Hz) was initially applied, followed by a 50 Hz notch filter. The filtered sEMG data were then segmented into windows of 300 sample points, with a 200 sample point overlap. The sEMG features, including the mean absolute value (MAV), waveform length, zero crossings, and slope sign changes, were extracted for each window [Li et al. \(2024\)](#). For the AUS data, the raw signal of each frame was processed sequentially through time gain compensation, bandpass

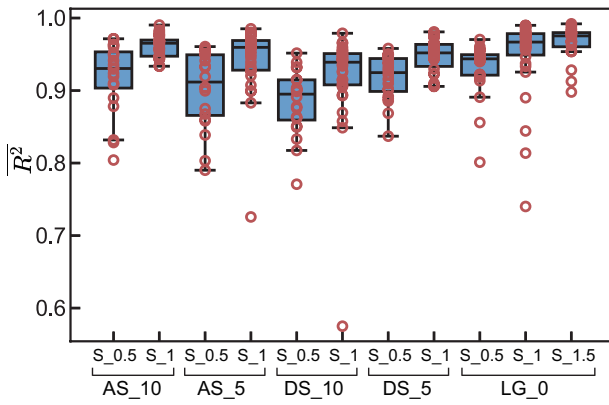


Figure 8. The evaluation of repeatability. The circles represent the R^2 between the average angle and joint angles for each participant across different ambulation modes. The box represents the distribution of R^2 for each movement.

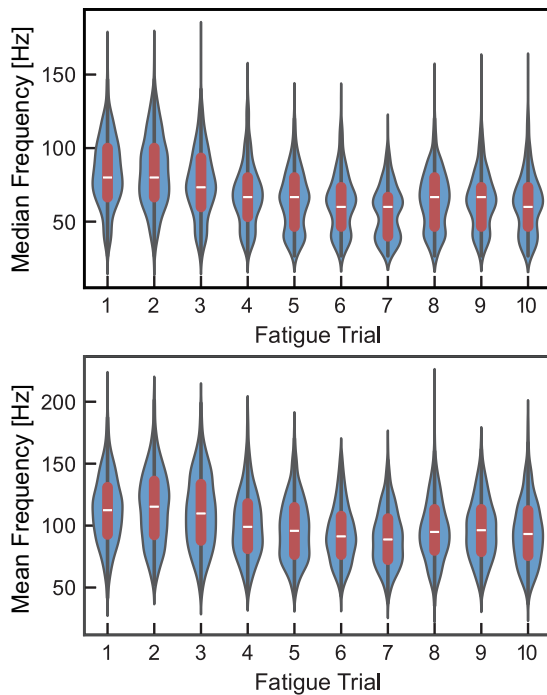


Figure 9. Violin plots depicting the distributions of the median frequency and mean frequency of RF in the left leg during gradual muscle fatigue trials.

filtering, envelope detection, and log compression Zeng et al. (2021). The frames were then segmented into a series of windows, each containing 20 sample points. The first and last 20 points were discarded prior to segmentation, as they typically do not contain valuable information, resulting in 48 segments per frame Yang et al. (2022). Two types of features are subsequently calculated for the AUS data: the MSD feature (mean and standard deviation) and the SFO feature (spatial first-order feature) Yang et al. (2019). Finally, the sEMG and AUS features were normalized via the Min-Max normalization method. Additionally, principal component analysis (PCA) was applied to the AUS feature sets to reduce

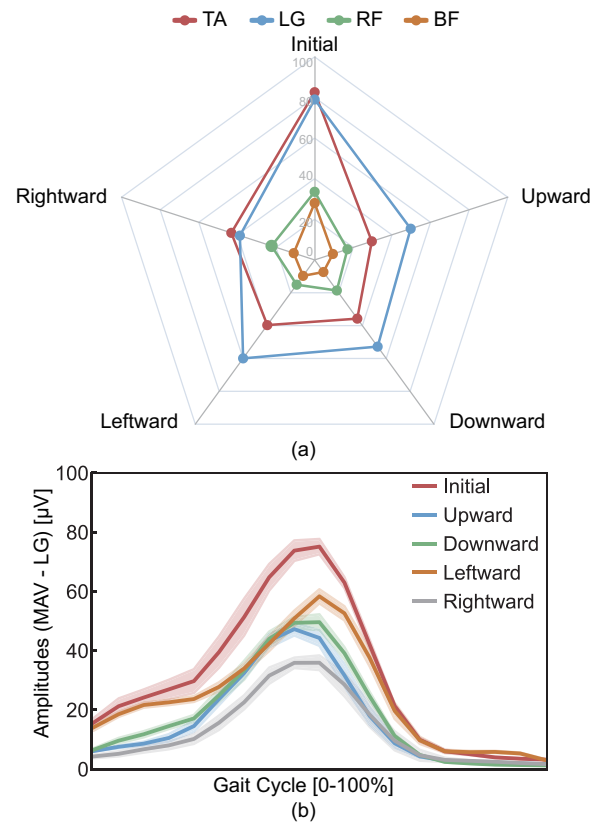


Figure 10. For the five shift positions: (a) the mean of the maximum MAV across all gait cycles for sEMG signals recorded from four muscles of the left leg; (b) MAV variation of the LG in the left leg throughout the gait cycle. The solid lines represent the average values across all cycles, whereas the shaded regions denote the standard deviation.

the dimension Yang et al. (2022). We employed 5-fold cross-validation, with each trial serving as one of the folds. The root mean square error (RMSE) was calculated for each participant to evaluate the regression performance.

To evaluate the performance of the sEMG, AUS, and multimodal fusion data, single-modal inputs used sEMG, MSD, and SFO features, respectively. The multimodal inputs included different feature fusion combinations: sEMG&MSD, sEMG&SFO, and MSD&SFO features. Figure 12 (a)–(f) shows the RMSE results for predicting the ankle, knee, and hip joint angles on the basis of different features. Among the predictions based on the sEMG features, the MLP demonstrated the best performance, achieving average RMSE values of 3.58° , 7.69° , and 5.49° for the ankle, knee, and hip joints, respectively. For the prediction based on MSD features, all three models exhibited similar performances, with average RMSE values of approximately 4.1° , 10.2° , and 5.8° for the ankle, knee, and hip joints, respectively. In the prediction based on SFO features, SVR showed a slight advantage, yielding average RMSE values of 4.08° , 10.12° , and 5.91° for the ankle, knee, and hip joints, respectively. Compared with single-modality

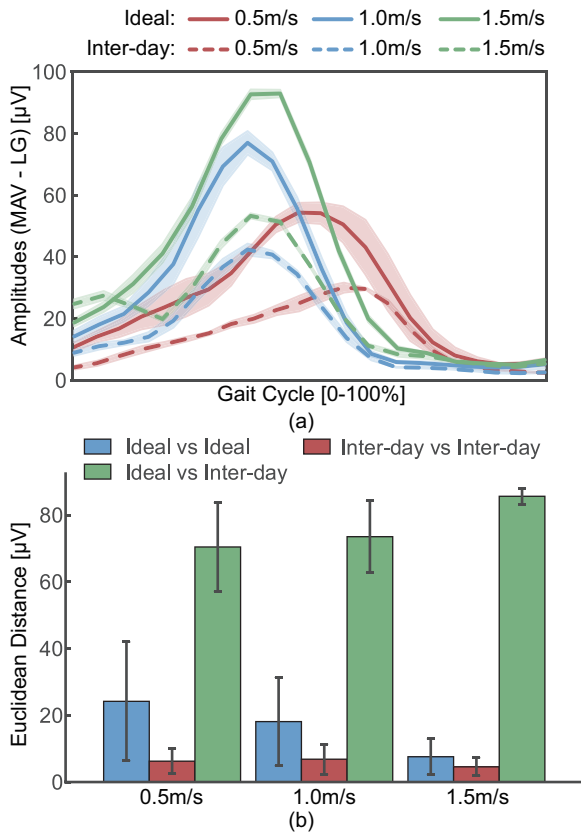


Figure 11. For ideal conditions and inter-day differences: (a) The variation in MAV values of the left leg LG throughout the gait cycle. The solid lines represent the average values across all gait cycles from five walking trials, whereas the shaded regions indicate the standard deviation. (b) Comparison of the Euclidean distance of MAV values for the left leg LG under two conditions: intra-condition trial comparisons and inter-condition trial comparisons. The bar height represents the mean value, and the error bars indicate the standard deviation.

features, the performance of the fusion of the sEMG&MSD and sEMG&SFO features was improved, resulting in smaller RMSE values. The performance enhancement for the sEMG&MSD and sEMG&SFO fusion features was particularly pronounced for the SVR and GPR models, with average RMSE values for the ankle, knee, and hip joint angles reduced to approximately 3.4° , 7.3° , and 4.3° , respectively. However, the combination of MSD&SFO features did not improve model performance, yielding RMSE values similar to those obtained from single MSD or SFO features. Therefore, combining different features of the same modality did not yield significant improvements. However, the fusion of sEMG and AUS signals, which incorporates both action potential information and thickness variation data from muscle contraction, demonstrates the potential of multimodal fusion for enhanced intent recognition. These results demonstrate the applicability of our dataset (K2MUSE) for lower limb joint angle estimation.

We evaluated recognition performance across three non-ideal conditions using sEMG features as input variables.

To effectively demonstrate the impact of these non-ideal conditions, we implemented testing protocols that deviated from conventional cross-validation approaches. For the electrode shifts, data from the initial position was used as the training dataset, while data from the other four shift positions served as the testing dataset. In the case of muscle fatigue, data from the first trial was designated as the training set, with data from the remaining nine trials used as testing dataset. For inter-day differences, data from the ideal condition experiments served as the training dataset, while data collected on a separate day was used as the testing dataset. The obtained angle prediction results are illustrated in Figure 12 (g), (h), and (i). Taking the MLP as an example, the RMSEs for the ankle, knee, and hip joints under electrode shifts, muscle fatigue, and inter-day differences are as follows: 5.36° , 11.36° , 8.88° ; 3.96° , 10.05° , 6.61° ; 8.73° , 19.67° , 11.92° . Compared to Figure 12 (a), the RMSEs under the three non-ideal conditions increase to varying extents, demonstrating the negative impact of non-ideal conditions on recognition performance. This observation is consistent with the analysis of MAV features presented in Section 5.5.

5.7 Comparison with public datasets

To evaluate the validity of the data from walking on different terrains, we compared the ankle, knee, and hip angles with two publicly available datasets. For the dataset from Reznick et al. (2021), the comparison includes walking data on various ramps, with all walking speeds set to 1.0 m/s. The participants in this dataset are healthy, with an average age of 30.5 years. In the dataset from Scherpereel et al. (2023), owing to differences in experimental paradigms, walking on ramps was compared at 1.0 m/s, whereas walking on level ground was compared at 1.2 m/s. The population in this dataset has an average age of 21.8 years, which is similar to that of our study.

We calculated the average values of our data, along with the cross-correlation coefficient (XCOR) and Pearson correlation coefficient (PCC), with the selected comparison datasets, as shown in Table 4. The results demonstrate that K2MUSE is highly correlated with previous studies. For the data from Reznick et al. (2021), the XCOR and PCC for joint angles range from 0.88 to 0.99 and from 0.93 to 0.99, respectively. Similarly, for the data from Scherpereel et al. (2023), the XCOR and PCC for joint angles range from 0.81 to 0.99 and from 0.90 to 0.99, respectively.

For walking tasks comparable to those in other datasets, we compared the trends in kinematic and kinetic variations. Compared with the dataset from Camargo et al. (2021), the

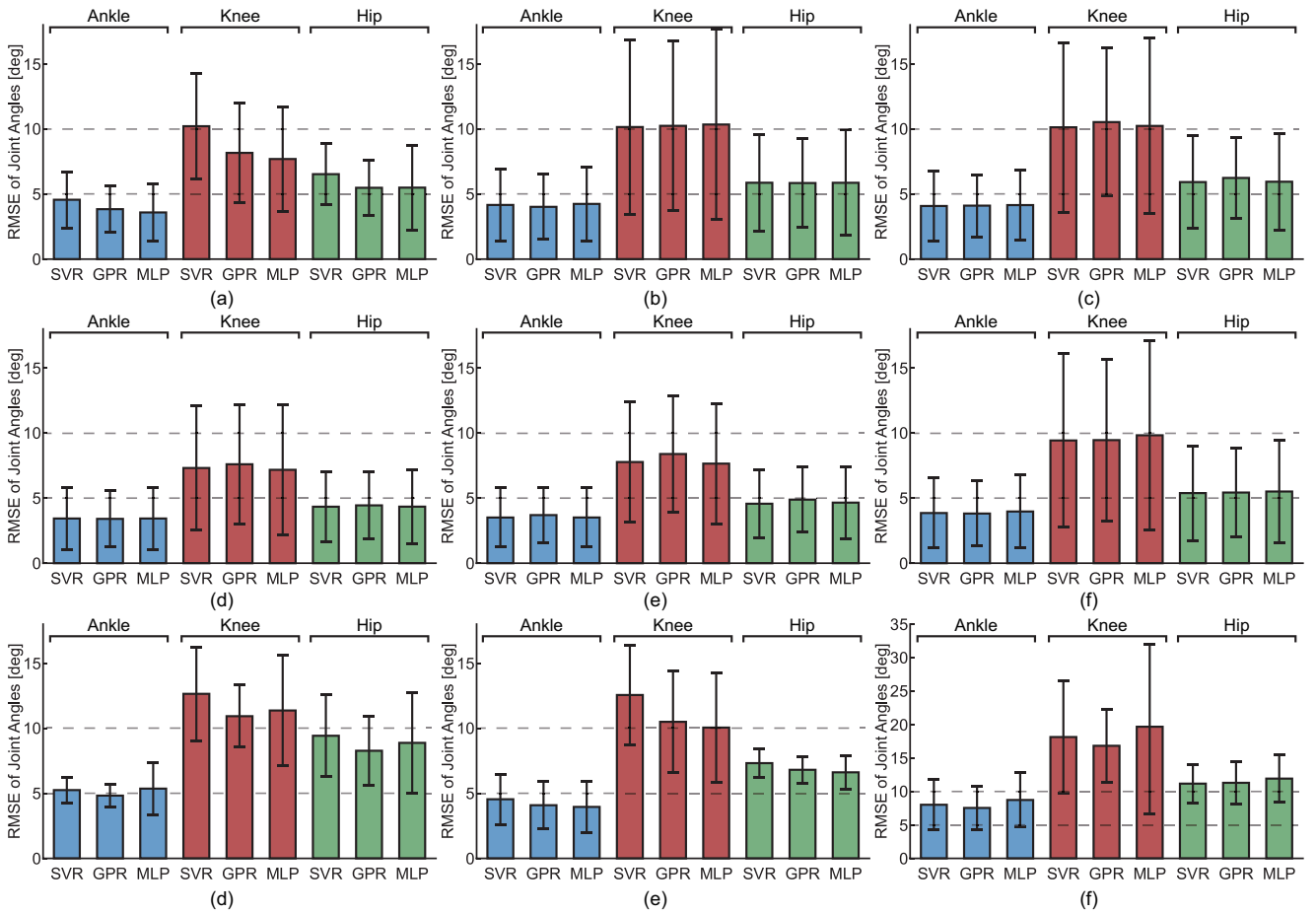


Figure 12. Regression results for angle estimation. (a), (b), and (c) show $RMSE$ with inputs of sEMG, MSD, and SFO features, respectively. (d), (e), and (f) show $RMSE$ with inputs of sEMG&MSD, sEMG&SFO, and MSD&SFO features, respectively. The height of the bars represents the mean value across all participants, whereas the error bars indicate the standard deviation. (g), (h), and (i) represent $RMSE$ for electrode shifts, muscle fatigue, and inter-day differences, respectively, with sEMG features as the input.

Table 4. Summary of the XCOR and PCC results between the K2MUSE dataset and the comparison datasets.

		LG_0			AS_5			AS_10			DS_5			DS_10		
		Ankle	Knee	Hip												
Reznick et al. (2021)	XCOR	0.93	0.98	0.99	0.93	0.97	0.99	0.98	0.97	0.98	0.90	0.97	0.96	0.88	0.97	0.90
	PCC	0.93	0.96	0.99	0.95	0.96	0.98	0.96	0.97	0.99	0.96	0.97	0.99	0.93	0.96	0.98
Scherpereel et al. (2023)	XCOR	0.82	0.99	0.99	0.82	0.99	0.99	0.91	0.99	0.99	0.81	0.99	0.98	0.81	0.99	0.98
	PCC	0.93	0.94	0.98	0.92	0.92	0.98	0.95	0.94	0.99	0.91	0.93	0.97	0.90	0.93	0.95

kinematic and kinetic variations in walking on level ground are similar. In kinematic analysis, the hip joint angle follows a nearly sinusoidal pattern, ranging from approximately 20° of flexion to 20° of extension. Similarly, the range of motion the ankle joint motion spans from 15° of dorsiflexion to 15° of plantar flexion, and the knee joint kinematics range from 0° to 60° . Additionally, similar trends in kinematics and kinetics are observed during walking on 5° ascending and descending ramps compared with Dimitrov et al. (2023).

5.8 Potential applications

Our dataset encompasses a diverse range of variables, comprehensively covering multiple terrains and acquisition

conditions. In biomechanical analysis, a wealth of kinematic, dynamic, and physiological data (sEMG, AUS) enables a comprehensive analysis of body movement performance from the perspective of motion mechanisms, particularly through the integration of muscle synergy d'Avella et al. (2003); Zhong et al. (2022). This rich dataset also provides valuable data support for big data-driven methods to uncover powerful solutions for intent decoding Jin et al. (2024); Wang et al. (2024). Additionally, the extensive human data in our dataset enable a more comprehensive evaluation of robotic performance. Currently, rehabilitation robots, such as exoskeletons, rely primarily on straps and similar mechanisms for physical interaction. However, the underlying interaction mechanism and mechanical

coupling often result in an expected assistance effect that is not fully transmitted, leading to an efficiency gap. By leveraging our dataset, this efficiency gap can be better analyzed and quantified, providing a solid foundation for optimizing exoskeleton design and improving overall assistive performance.

In bionic design for robots, as shown in Figure 13 (a)–(c), exoskeletons are evolving toward a rigid-flexible coupling approach, progressing from joint assistance with elastic actuators [Chen et al. \(2024a\)](#) to muscle assistance via tendon-driven mechanisms [Tan et al. \(2022\)](#), and further toward bioinspired design optimization [Liu et al. \(2024\)](#). To increase their effectiveness, the system design of rehabilitation robots should align with actual biomechanics, ensuring that actuation effects conform to physiological principles. K2MUSE not only provides comprehensive data on joint and limb movements but also captures physiological changes in muscle contraction, enabling the development of more ergonomic and biomimetic robotic designs. In terms of controller design for robots, handling variations in terrains and movement patterns requires adaptable control strategies. In Figure 13 (d), an end-to-end controller built upon the dataset can dynamically adjust to changing motion tasks while ensuring scalability [Molinaro et al. \(2024b\)](#). In Figure 13 (e) and (f), without relying on manual tuning or predefined control laws, these controllers can be generalized to a wider range of tasks as the dataset expands, increasing their adaptability and robustness in real-world applications [Molinaro et al. \(2024a\)](#); [Luo et al. \(2024\)](#).

5.9 Data limitations

Given that the dataset involved multiple acquisition systems and extensive data collection sessions, only data from female participants walking at 1.0 m/s on different ramps were included. Owing to recruitment limitations, the participant diversity in this dataset is restricted, preventing the data from fully representing the entire population. Additionally, some trials from certain participants contained defective data due to an investigator error, which was later recollected.

6 Usage notes

MATLAB and Python scripts are provided to assist users in visualizing and utilizing data. These scripts provide instructions for loading data from the ‘ProcessedData’ folder, generating plots, and performing joint angle estimation via machine learning models. For additional details on data usage, please refer to the README file. The metadata in the ‘*.c3d’ files can



Figure 13. Innovative exploration of various exoskeleton designs and control strategies: (a) hip-knee-ankle exoskeleton with series elastic actuators; (b) soft exosuit; (c) ligaments-inspired knee exoskeleton; (d) task-agnostic exoskeleton control; (e) unified exoskeleton control; (f) sim2real framework for the exoskeleton.

be directly accessed via [the open-source software Mokka](#). Alternatively, the open-source and cross-platform library [Biomechanics ToolKit \(BTK\)](#) can also be used to parse ‘*.c3d’ files.

7 Code availability

The dataset and codes used to process the data can be found at [Kaggle – K2MUSE: A Human Lower Limb Multimodal Dataset](#). The data can be accessed via MATLAB, and a description of the dataset hierarchy is available at <https://k2muse.github.io/datasets/>. The joint angle estimation, based on machine learning models, is implemented via Python.

- `scriptProcess.mlx` is used to extract and parse data collected from different devices in the ‘SourceData’ folder and save the data in a unified format.
- `scriptPlot.mlx` is used to plot graphs showing the changes in joint angles and moments during the gait cycle in gait analysis.
- `recognitionDemo.ipynb` is designed for processing sEMG, AUS, and kinematic data, building machine learning models, and analyzing the results.

8 Conclusion and future work

In this paper, we presented the K2MUSE dataset, a large-scale lower limb dataset that includes 3D motion trajectories, ground reaction forces, amplitude-mode ultrasound, and sEMG data. We collected data across up to 20 different ambulation conditions, including different speeds, inclines, and nonideal conditions. By comparing our dataset with existing public datasets, we evaluated and analyzed the quality and validity of the dataset. K2MUSE provides a comprehensive data resource for the development of natural interaction control algorithms and human motion recognition in rehabilitation robotics.

In the future, we plan to expand the scope of K2MUSE by incorporating additional walking tasks, such as sit-to-stand and sit-to-walk transitions [Huo et al. \(2021\)](#), as well as broader walking environments, including outdoor settings and stairs. We also aim to include a larger participant pool, such as stroke patients. Furthermore, we will gather walking data while wearing assistive robots, enabling comparative analysis with natural walking patterns. We believe these efforts will further advance the development of rehabilitation robots, and we look forward to the creation of algorithms based on this dataset that can achieve embodied intelligence in robots in future research.

Acknowledgements

The authors extend their gratitude to all the volunteers and colleagues who contributed to the experiments for this dataset. The authors also appreciate the development and experimental support provided by the State Key Laboratory of Robotics, Shenyang Institute of Automation, Chinese Academy of Sciences.

Declaration of conflicting interests

The author(s) declare no potential conflicts of interest with respect to the research, authorship, and/or publication of this article.

Funding

The author(s) disclosed receipt of the following financial support for the research, authorship, and/or publication of this article: This work was supported in part by the National Natural Science Foundation of China under Grants 62473361, 62333007, and U22A2067; in part by the Natural Science Foundation of Liaoning Province under Grant 2025JH6/101000028; in part by the Fundamental Research Project of SIA under Grant 2024JC1K01; and in part by the China Postdoctoral Science Foundation under Grant 2024M753412.

ORCID iDs

Jiwei Li  <https://orcid.org/0009-0000-2297-8278>
 Bi Zhang  <https://orcid.org/0000-0001-8001-002X>
 Xiaowei Tan  <https://orcid.org/0000-0003-0990-0323>
 Wanxin Chen  <https://orcid.org/0000-0001-5930-0209>
 Zhaoyuan Liu  <https://orcid.org/0009-0002-5195-6128>
 Juanjuan Zhang  <https://orcid.org/0000-0002-3833-487X>
 Weiguang Huo  <https://orcid.org/0000-0002-7370-5189>
 Jian Huang  <https://orcid.org/0000-0002-6267-8824>
 Lianqing Liu  <https://orcid.org/0000-0003-1329-1487>
 Xingang Zhao  <https://orcid.org/0000-0001-8194-1870>

References

- Bovi G, Rabuffetti M, Mazzoleni P and Ferrarin M (2011) A multiple-task gait analysis approach: kinematic, kinetic and emg reference data for healthy young and adult subjects. *Gait & posture* 33(1): 6–13.
- Brantley JA, Luu TP, Nakagome S, Zhu F and Contreras-Vidal JL (2018) Full body mobile brain-body imaging data during unconstrained locomotion on stairs, ramps, and level ground. *Scientific data* 5(1): 1–10.
- Camargo J, Ramanathan A, Flanagan W and Young A (2021) A comprehensive, open-source dataset of lower limb biomechanics in multiple conditions of stairs, ramps, and level-ground ambulation and transitions. *Journal of Biomechanics* 119: 110320.
- Chandra S, Hayashibe M and Thoniyath A (2018) Muscle fatigue induced hand tremor clustering in dynamic laparoscopic manipulation. *IEEE Transactions on Systems, Man, and Cybernetics: Systems* 50(12): 5420–5431.
- Chen W, Zhang B, Tan X, Zhao Y, Liu L and Zhao X (2024a) Hip–knee–ankle rehabilitation exoskeleton with compliant actuators: From human–robot interaction control to clinical evaluation. *IEEE Transactions on Robotics* .
- Chen Y, Miao S, Chen G, Ye J, Fu C, Liang B, Song S and Li X (2024b) Learning to assist different wearers in multitasks: efficient and individualized human-in-the-loop adaptation framework for lower-limb exoskeleton. *IEEE Transactions on Robotics* .
- d'Avella A, Saltiel P and Bizzi E (2003) Combinations of muscle synergies in the construction of a natural motor behavior. *Nature neuroscience* 6(3): 300–308.
- David PF, David RC, Diego T et al. (2023) Human locomotion databases: a systematic review. *IEEE Journal of Biomedical and Health Informatics* 28(3): 1716–1729.
- Davis III RB, Ounpuu S, Tyburski D and Gage JR (1991) A gait analysis data collection and reduction technique. *Human*

- movement science* 10(5): 575–587.
- Dick TJ, Biewener AA and Wakeling JM (2017) Comparison of human gastrocnemius forces predicted by hill-type muscle models and estimated from ultrasound images. *Journal of experimental biology* 220(9): 1643–1653.
- Dimitrov H, Bull AM and Farina D (2023) High-density emg, imu, kinetic, and kinematic open-source data for comprehensive locomotion activities. *Scientific Data* 10(1): 789.
- Ding Y, Kim M, Kuindersma S and Walsh CJ (2018) Human-in-the-loop optimization of hip assistance with a soft exosuit during walking. *Science robotics* 3(15): eaar5438.
- Divekar NV, Thomas GC, Yerva AR, Frame HB and Gregg RD (2024) A versatile knee exoskeleton mitigates quadriceps fatigue in lifting, lowering, and carrying tasks. *Science Robotics* 9(94): eadr8282.
- Elery T, Rezazadeh S, Nesler C and Gregg RD (2020) Design and validation of a powered knee–ankle prosthesis with high-torque, low-impedance actuators. *IEEE Transactions on Robotics* 36(6): 1649–1668.
- Fukuchi CA, Fukuchi RK and Duarte M (2018) A public dataset of overground and treadmill walking kinematics and kinetics in healthy individuals. *PeerJ* 6: e4640.
- Gorton III GE, Hebert DA and Gannotti ME (2009) Assessment of the kinematic variability among 12 motion analysis laboratories. *Gait & posture* 29(3): 398–402.
- Grood ES and Suntay WJ (1983) A joint coordinate system for the clinical description of three-dimensional motions: Application to the knee. *Journal of Biomechanical Engineering* 105(2): 136–144.
- He Y, Luu TP, Nathan K, Nakagome S and Contreras-Vidal JL (2018) A mobile brain-body imaging dataset recorded during treadmill walking with a brain-computer interface. *Scientific data* 5(1): 1–10.
- Hermens HJ, Freriks B, Disselhorst-Klug C and Rau G (2000) Development of recommendations for semg sensors and sensor placement procedures. *Journal of electromyography and Kinesiology* 10(5): 361–374.
- Hu B, Rouse E and Hargrove L (2018) Benchmark datasets for bilateral lower-limb neuromechanical signals from wearable sensors during unassisted locomotion in able-bodied individuals. *Frontiers in Robotics and AI* 5: 14.
- Huo W, Moon H, Alouane MA, Bonnet V, Huang J, Amirat Y, Vaidyanathan R and Mohammed S (2021) Impedance modulation control of a lower-limb exoskeleton to assist sit-to-stand movements. *IEEE Transactions on Robotics* 38(2): 1230–1249.
- Jin Y, Alvarez JT, Suitor EL, Swaminathan K, Chin A, Civici US, Nuckols RW, Howe RD and Walsh CJ (2024) Estimation of joint torque in dynamic activities using wearable a-mode ultrasound. *Nature Communications* 15(1): 5756.
- Kainz H, Graham D, Edwards J, Walsh HP, Maine S, Boyd RN, Lloyd DG, Modenese L and Carty CP (2017) Reliability of four models for clinical gait analysis. *Gait & posture* 54: 325–331.
- Kang I, Hsu H and Young A (2019) The effect of hip assistance levels on human energetic cost using robotic hip exoskeletons. *IEEE Robotics and Automation Letters* 4(2): 430–437.
- Lencioni T, Carpinella I, Rabuffetti M, Marzegan A and Ferrarin M (2019) Human kinematic, kinetic and emg data during different walking and stair ascending and descending tasks. *Scientific data* 6(1): 309.
- Li J, Zhang B, Chen W, Bu C, Zhao Y and Zhao X (2024) Improving hand gesture recognition robustness to dynamic posture variations by multimodal deep feature fusion. *IEEE Transactions on Neural Systems and Rehabilitation Engineering* .
- Liu Z, Han J, Han J and Zhang J (2024) Design and evaluation of a lightweight, ligaments-inspired knee exoskeleton for walking assistance. *IEEE Robotics and Automation Letters* .
- Luo S, Jiang M, Zhang S, Zhu J, Yu S, Dominguez Silva I, Wang T, Rouse E, Zhou B, Yuk H et al. (2024) Experiment-free exoskeleton assistance via learning in simulation. *Nature* 630(8016): 353–359.
- Luo Y, Coppola SM, Dixon PC, Li S, Dennerlein JT and Hu B (2020) A database of human gait performance on irregular and uneven surfaces collected by wearable sensors. *Scientific data* 7(1): 219.
- Molinaro DD, Kang I and Young AJ (2024a) Estimating human joint moments unifies exoskeleton control, reducing user effort. *Science Robotics* 9(88): eadi8852.
- Molinaro DD, Scherpereel KL, Schonhaut EB, Evangelopoulos G, Shepherd MK and Young AJ (2024b) Task-agnostic exoskeleton control via biological joint moment estimation. *Nature* 635(8038): 337–344.
- Moreira L, Figueiredo J, Fonseca P, Vilas-Boas JP and Santos CP (2021) Lower limb kinematic, kinetic, and emg data from young healthy humans during walking at controlled speeds. *Scientific data* 8(1): 103.
- Novacheck TF (1998) The biomechanics of running. *Gait & posture* 7(1): 77–95.
- Nuckols RW, Lee S, Swaminathan K, Orzel D, Howe RD and Walsh CJ (2021) Individualization of exosuit assistance based on measured muscle dynamics during versatile walking. *Science robotics* 6(60): eabj1362.
- Ortiz M, de la Ossa L, Juan J, Iáñez E, Torricelli D, Tórner J and Azorín JM (2023) An eeg database for the cognitive assessment of motor imagery during walking with a lower-limb

- exoskeleton. *Scientific Data* 10(1): 343.
- Perera CK, Hussain Z, Khant M, Gopalai AA, Gouwanda D and Ahmad SA (2024) A motion capture dataset on human sitting to walking transitions. *Scientific Data* 11(1): 878.
- Quintero D, Villarreal DJ, Lambert DJ, Kapp S and Gregg RD (2018) Continuous-phase control of a powered knee–ankle prosthesis: Amputee experiments across speeds and inclines. *IEEE Transactions on Robotics* 34(3): 686–701.
- Rabuffetti M, Marzegan A, Crippa A, Carpinella I, Lencioni T, Castagna A and Ferrarin M (2019) The lamb gait analysis protocol: Definition and experimental assessment of operator-related variability. *Proceedings of the Institution of Mechanical Engineers, Part H: Journal of engineering in medicine* 233(3): 342–353.
- Reznick E, Embry KR, Neuman R, Bolívar-Nieto E, Fey NP and Gregg RD (2021) Lower-limb kinematics and kinetics during continuously varying human locomotion. *Scientific Data* 8(1): 282.
- Riener R, Rabuffetti M and Frigo C (2002) Stair ascent and descent at different inclinations. *Gait & posture* 15(1): 32–44.
- Scherpereel K, Molinaro D, Inan O, Shepherd M and Young A (2023) A human lower-limb biomechanics and wearable sensors dataset during cyclic and non-cyclic activities. *Scientific Data* 10(1): 924.
- Schulte RV, Prinsen EC, Schaake L, Paassen RP, Zondag M, van Staveren ES, Poel M and Buurke JH (2023) Database of lower limb kinematics and electromyography during gait-related activities in able-bodied subjects. *Scientific Data* 10(1): 461.
- Schwartz MH, Rozumalski A and Trost JP (2008) The effect of walking speed on the gait of typically developing children. *Journal of biomechanics* 41(8): 1639–1650.
- Sharma A, Rai V, Calvert M, Dai Z, Guo Z, Boe D and Rombokas E (2023) A non-laboratory gait dataset of full body kinematics and egocentric vision. *Scientific Data* 10(1): 26.
- Simonlehner M, Dumphart B and Horsak B (2024) Gaitrec-vr: 3d gait analysis for walking overground with and without a head-mounted-display in virtual reality. *Scientific Data* 11(1): 1099.
- Slade P, Kochenderfer MJ, Delp SL and Collins SH (2022) Personalizing exoskeleton assistance while walking in the real world. *Nature* 610(7931): 277–282.
- Tan X, Zhang B, Liu G, Zhao X and Zhao Y (2022) A time-independent control system for natural human gait assistance with a soft exoskeleton. *IEEE Transactions on Robotics* 39(2): 1653–1667.
- CMU Motion Capture Database (2024) [CMU Graphics Lab Motion Capture Database](#). Accessed: 2024-12-10.
- Vicon Motion Systems, Inc (2024a) [Nexus 2.16 documentation: Vicon Nexus User Guide, Modeling with Plug-in](#). Accessed: 2024-12-10.
- Vicon Motion Systems, Inc (2024b) [Nexus 2.16 documentation: Plug-in Gait Reference Guide](#). Accessed: 2024-12-10.
- Van Criekinge T, Saeys W, Truijien S, Vereeck L, Sloot LH and Halleman A (2023) A full-body motion capture gait dataset of 138 able-bodied adults across the life span and 50 stroke survivors. *Scientific data* 10(1): 852.
- Wang C, Chen X, Wang L, Makihata M, Liu HC, Zhou T and Zhao X (2022) Bioadhesive ultrasound for long-term continuous imaging of diverse organs. *Science* 377(6605): 517–523.
- Wang G, Jin L, Zhang J, Duan X, Yi J, Zhang M and Sun Z (2024) Recurrent neural network enabled continuous motion estimation of lower limb joints from incomplete semg signals. *IEEE Transactions on Neural Systems and Rehabilitation Engineering* .
- Weber D and Matsiko A (2023) Assistive robotics should seamlessly integrate humans and robots.
- Wei S, Zhang Y and Liu H (2022) A multimodal multilevel converged attention network for hand gesture recognition with hybrid semg and a-mode ultrasound sensing. *IEEE transactions on cybernetics* 53(12): 7723–7734.
- Wei W, Tan F, Zhang H, Mao H, Fu M, Samuel OW and Li G (2023) Surface electromyogram, kinematic, and kinetic dataset of lower limb walking for movement intent recognition. *Scientific Data* 10(1): 358.
- Wolpert DM and Kawato M (1998) Multiple paired forward and inverse models for motor control. *Neural networks* 11(7-8): 1317–1329.
- Wu Q, Xi C, Ding L, Wei C, Ren H, Law R, Dong H and Li XL (2016) Classification of emg signals by bfa-optimized gsvcm for diagnosis of fatigue status. *IEEE Transactions on Automation Science and Engineering* 14(2): 915–930.
- Yang X, Sun X, Zhou D, Li Y and Liu H (2018) Towards wearable a-mode ultrasound sensing for real-time finger motion recognition. *IEEE Transactions on Neural Systems and Rehabilitation Engineering* 26(6): 1199–1208.
- Yang X, Yan J, Chen Z, Ding H and Liu H (2019) A proportional pattern recognition control scheme for wearable a-mode ultrasound sensing. *IEEE Transactions on Industrial Electronics* 67(1): 800–808.
- Yang X, Yan J, Yin Z and Liu H (2022) Sonomyographic prosthetic interaction: Online simultaneous and proportional control of wrist and hand motions using semisupervised learning. *IEEE/ASME Transactions on Mechatronics* 28(2): 804–813.

- Yang X, Zhou Y and Liu H (2020) Wearable ultrasound-based decoding of simultaneous wrist/hand kinematics. *IEEE Transactions on Industrial Electronics* 68(9): 8667–8675.
- Young AJ and Ferris DP (2016) State of the art and future directions for lower limb robotic exoskeletons. *IEEE Transactions on Neural Systems and Rehabilitation Engineering* 25(2): 171–182.
- Zeng J, Zhou Y, Yang Y, Yan J and Liu H (2021) Fatigue-sensitivity comparison of semg and a-mode ultrasound based hand gesture recognition. *IEEE Journal of Biomedical and Health Informatics* 26(4): 1718–1725.
- Zhang J, Fiers P, Witte KA, Jackson RW, Poggensee KL, Atkeson CG and Collins SH (2017) Human-in-the-loop optimization of exoskeleton assistance during walking. *Science* 356(6344): 1280–1284.
- Zhong W, Fu X and Zhang M (2022) A muscle synergy-driven anfis approach to predict continuous knee joint movement. *IEEE Transactions on Fuzzy Systems* 30(6): 1553–1563.
- Zhu B, Zhang D, Chu Y, Gu Y and Zhao X (2022) Senic: An open source dataset for semg-based gesture recognition in non-ideal conditions. *IEEE Transactions on Neural Systems and Rehabilitation Engineering* 30: 1252–1260.